# Nonlinear optics in diamond-fin photonic nanowires: soliton formation and frequency comb generation

VICTOR M. FERNANDEZ LAGUNA[1,3,*] AND NICOLAE C. PANOIU[2,4]

[1]*Airbus Defence and Space, Gunnels Wood Road, Stevenage SG1 2AS, UK*
[2]*Department of Electronic and Electrical Engineering, University College London, Torrington Place, London WC1E 7JE, UK*
[3]*victor.v.fernandez@airbus.com*
[4]*n.panoiu@ucl.ac.uk*
[*]*victor.laguna.15@ucl.ac.uk*

**Abstract:** We present a detailed study of the nonlinear optical properties of newly developed subwavelength diamond-fin waveguides, along with an analysis of soliton generation and pulse spectral broadening in these structures. Our rigorous mathematical model includes all the key linear and nonlinear optical effects that govern the pulse dynamics in these diamond waveguides. As a relevant application of our investigations, we demonstrate how these waveguides can be employed to efficiently generate frequency combs in the visible spectral domain.

## 1. Introduction

Synthetic diamond is becoming an increasingly fashionable material platform for on-chip optical communications, particularly due to its attractive classical and quantum optical properties [1–3]. Central among these remarkable optical properties are its large transparency window, ranging from ultraviolet (UV) to far-infrared (IR), very small optical absorption losses, and it can be synthesized with a high refractive index, $n_{di} \approx 2.4$, thus enabling enhanced optical waveguides mode confinement in a broad spectral range extending from 500 nm to 1000 nm. Equally important for its applications to active photonic devices, diamond possesses key nonlinear optical properties, including large Kerr nonlinearity that can be employed to frequency conversion and comb generation devices, and also strong Raman interaction at the operating wavelengths of ~2 μm and with pump laser wavelengths in the telecom band at around ~1.6 μm [4]. These important optical properties are accompanied by excellent thermal properties, synthetic diamond being good thermal conductor with low thermo-optic coefficient and low thermal expansion coefficient, properties that render it an ideal material for high-power applications and integration of electro-optic systems. In addition, due to the numerous color centers of diamond, which potentially can be precisely controlled, this material has emerged as a promising low-temperature platform for quantum computing, perhaps one of the future core applications of diamond [5].

The functionality of diamond is greatly broadened by the fact that photonic structures with subwavelength features, such as subwavelength waveguides, can be readily implemented in this platform (for a review of optical properties of subwavelength waveguides the reader is referred to [6]). This enables dispersion-engineered devices and applications in the visible spectrum and therefore makes diamond photonics an appealing alternative to well-established, more mature photonic platforms, such as silicon-on-insulator [7], silicon nitride [8], or compound semiconductor on-insulator [9]. For example, subwavelength diamond waveguides would enable the development of photonic systems that incorporate cheaper light sources, such as vertical-cavity

surface-emitting lasers (VCSELs) at 850 nm, which are extensively used in data centers [10]. Moreover, the relatively large nonlinear refractive index coefficient of diamond in the visible spectrum, i.e. $n_2 = 1.3 \times 10^{-19}$ m$^2$ W$^{-1}$ [3], in conjunction with the fact that it has an extremely small two-photon absorption coefficient, would enable the implementation of high quality-factor, temperature-insensitive, microring resonators [11] for the efficient generation of frequency combs in these frequency bands. This would further increase the interest in on-chip frequency comb generation [12], which is a key functionality widely employed in microwave photonic signal generation and wavelength-division multiplexing systems [13–15].

Motivated by these ideas, here we study pulsed dynamics in subwavelength diamond-fin waveguides, a recently developed type of diamond waveguide which, apart from the advantages already highlighted, could improve the seamless integration with very large-scale integration (VLSI) electronics for on-chip optical communications [16]. More specifically, we demonstrate that diamond-fin waveguides can be designed to possess zero group-velocity dispersion (GVD) points, thus enabling soliton formation and efficient supercontinuum generation in ultracompact photonic devices, the latter being recently demonstrated [17]. To illustrate the versatility of this type of optical waveguide, we demonstrate that frequency comb generation can be readily implemented using such photonic structures.

The article is organized as follows. In the next section we present the structure of the investigated waveguide and the frequency dispersion properties of its optical modes. Then, in Section 3, we introduce a theoretical model that describes the optical pulse dynamics upon propagation in diamond fin waveguides. Furthermore, in Section 4 we discuss two applications of our diamond fin waveguides, namely soliton formation and frequency comb generation. Finally, in the last section we summarize the main conclusions of our study.

## 2. Waveguide structure and mode dispersion properties

The waveguide considered in this work, and which has been proposed in [16], is schematically shown in Fig. 1(a). It is a single-mode uniform waveguide consisting of a diamond substrate, from which a diamond light guiding fin of width $w$ rises to a height $h_{fin} = h_b + t + h$. A silicon dioxide buffer layer is grown from the substrate up to height $h_b$, above which the edge of the fin wall rises by $t + h$, where $t$ is the thickness of a silicon nitride layer used to increase the refractive index contrast and thus enhance the field confinement.
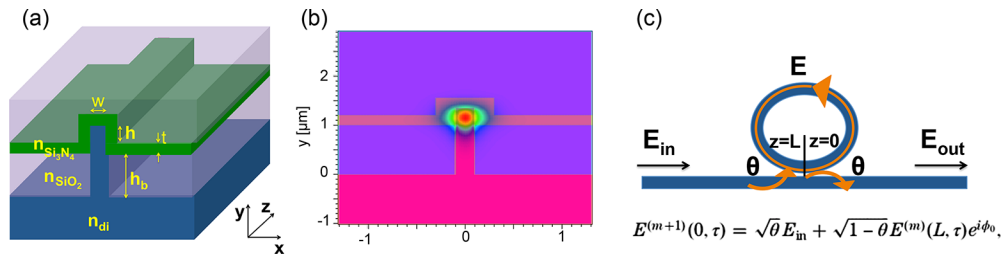


**Fig. 1.** (a) Schematics of a diamond fin waveguide. (b) Spatial profile of the $E_x$-component of the quasi-TE mode supported by the optical waveguide. (c) Photonic circuit model for the frequency comb generation, including the cavity boundary conditions.

With buffer layers thicker than about 1 µm, the propagation losses due to substrate leakage can be reduced below 0.15 dB cm$^{-1}$ [16]. In Fig. 1(b), we show the waveguide cross-section with $h_b = 1$ µm, $h = 350$ nm, $t = 200$ nm, and $w = 200$ nm. For these waveguide parameters, we employed the finite-element method implemented in Synopsys's commercially available software FemSIM [19] to compute the optical guiding modes supported by the structure. The spatial

profile of the dominant component ($E_x$) of the quasi-TE mode, calculated for $\lambda$ = 637 nm, is also depicted in Fig. 1(b). At this wavelength, the effective refractive index is $n_{eff}$ = 2.129.

We investigate four waveguide designs, labeled *A*, *B*, *C*, and *D*, defined by the parameters: *w* was 200 nm, 300 nm, 400 nm, and 500 nm, *h* was 350 nm, 350 nm, 500 nm, and 600 nm, and $h_b$ was 1 µm, 2.2 µm, 3.5 µm, and 7 µm, respectively. In practice, waveguides with aspect ratios as large as 10:1 can be readily fabricated using anisotropic inductively coupled plasma reactive ion etching, so that our choice for the waveguide configuration is relevant from a practical point of view. For all these cases we computed the following waveguide dispersion coefficients: the first-order dispersion coefficient, $\beta_1 = d\beta/d\omega = 1/v_g$, where $\beta$ and $v_g$ are the propagation constant and group-velocity (GV), respectively, the GVD coefficient, $\beta_2 = d^2\beta/d\omega^2$, and the third-order dispersion (TOD) coefficient, $\beta_3 = d^3\beta/d\omega^3$; the frequency dependence of these coefficients are plotted in Fig. 2.
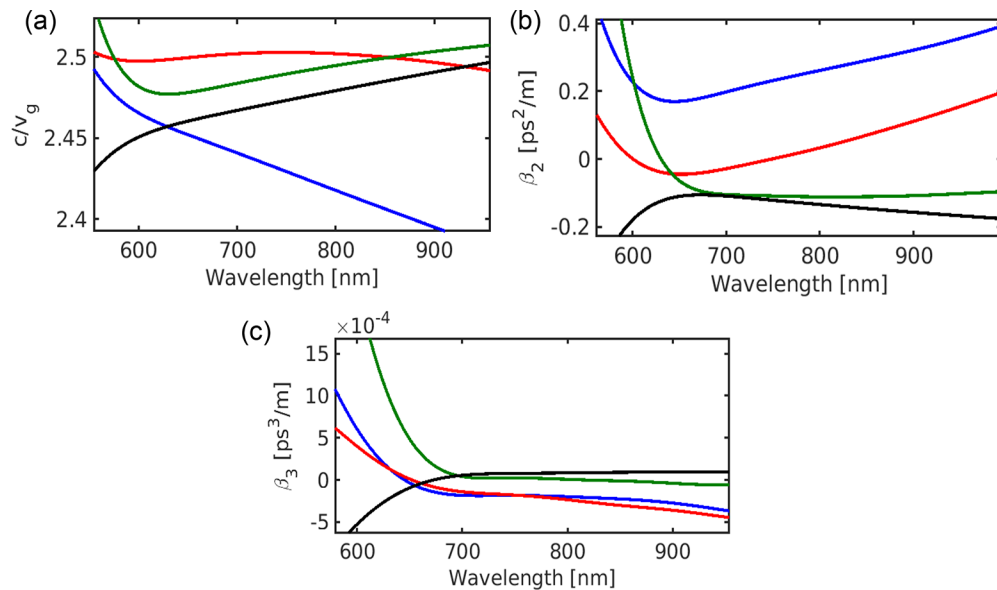


**Fig. 2.** (a), (b), (c) Group index, second-order dispersion coefficient, and third-order dispersion coefficient, respectively, determined for four diamond-fin waveguides. The colors blue, red, green, and black correspond to the designs *A*, *B*, *C*, and *D*, respectively, described in the text of the paper.

Figure 2(b) deserves particular attention as it illustrates that it is possible to design waveguides with $\beta_2 < 0$ (e.g. waveguides *B*, *C*, and *D*), which can support soliton propagation and efficient four-wave mixing, as well as waveguides that possess zero-GVD points defined by $\beta_2(\omega) = 0$ (e.g. waveguides *B* and *C*), which enable efficient supercontinuum generation. Especially of interest is the waveguide *B*, since it shows the smallest $v_g$ for the widest wavelength range, which suggests it provides broadband enhanced Kerr nonlinearity.

A sensitivity analysis of the effective index on the key design parameters was performed in order to show the tolerance against potential fabrication errors. The dependence of the effective index on waveguide width and buffer height, determined for designs *B* and *C*, are plotted in Figs. 3(a), 3(b) and 3(c), 3(d), respectively. The results summarized in these plots suggest that the variation of the effective index and, consequently, of the waveguide mode, is very small for both waveguides *B* and *C*. Note that, in this study, the wavelength is fixed to 750 nm; in addition, the width used for the study of the impact of height variations is the nominal width for each

waveguide as detailed earlier, and similar applies for the analysis of the variation of the width, *e.g.* the height employed is the nominal value for each waveguide.
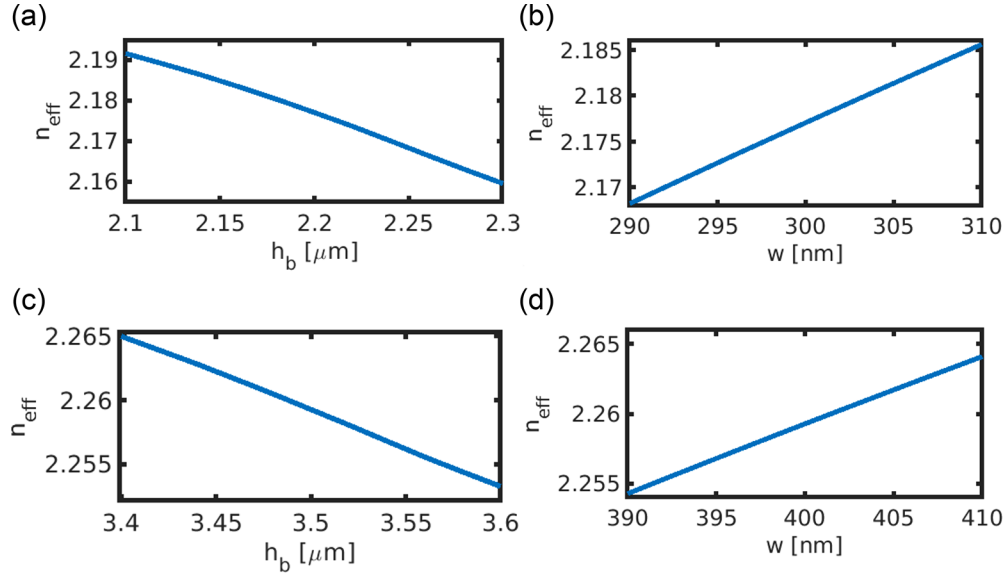


**Fig. 3.** Dependence of the effective index on the waveguide width $w$ and buffer height $h_b$, determined for the designs $B$ (top panels) and $C$ (bottom panels).

## 3. Theoretical model and simulation of pulse dynamics

Within the standard slowly-varying envelope approximation, the pulse dynamics in the diamond-fin waveguide is described by the well-known nonlinear Schrödinger equation (NLSE):

$$i\left(\frac{\partial u}{\partial z} - \frac{1}{v_g T_0}\frac{\partial u}{\partial \tau}\right) - \frac{\beta_2}{2T_0^2}\frac{\partial^2 u}{\partial \tau^2} - i\frac{\beta_3}{6T_0^3}\frac{\partial^3 u}{\partial \tau^3} + i\frac{c\kappa\alpha_{in}}{2n_{di}v_g}u + \gamma P_0|u|^2 u = 0, \qquad (1)$$

where $\tau = t/T_0$ and $u = a(z,\tau)/\sqrt{P_0}$, with $t$, $z$, and $a$ being the time, propagation distance, and pulse envelope, respectively, and $T_0$ and $P_0$ are the input pulse width and peak power, respectively. In Eq. (1), $\alpha_{in} = 1$ cm$^{-1}$ is the intrinsic loss of diamond [1], $\kappa$ is an overlap integral and $\gamma$ is the nonlinear waveguide coefficient. These quantities are defined as [20,21]:

$$\kappa = \frac{\epsilon_0 n_{di}^2}{2W}\int_{S_{wg}}|\mathbf{e}(\omega)|^2 dS, \qquad (2a)$$

$$\gamma = \frac{3\omega\epsilon_0}{16v_g^2}\frac{1}{W^2}\int_{S_{wg}}\mathbf{e}^*(\omega)\hat{\chi}^{(3)}(\omega)\!:\!\mathbf{e}(\omega)\mathbf{e}^*(\omega)\mathbf{e}(\omega)dS, \qquad (2b)$$

where $\mathbf{e}(\mathbf{r};\omega)$ is the electric field component of the optical mode, $W$ the energy density of the mode, and $\hat{\chi}^{(3)}(\omega) \equiv \hat{\chi}^{(3,e)}(\omega; \omega, -\omega, \omega)$ is the the third-order (electronic) susceptibility tensor of diamond. As diamond has cubic crystal lattice, $\hat{\chi}^{(3)}$ has three independent components. The relationships between these 3 independent components are $\hat{\chi}^{(3)}_{1111} = 3\hat{\chi}^{(3)}_{1221} = 3\hat{\chi}^{(3)}_{1122}$ [1], so that in the case of diamond $\hat{\chi}^{(3)}$ has only one independent component. The corresponding Kerr coefficient is similar or larger than that of commonly used nonlinear optical materials, *e.g.* silica ($n_2 \sim 2.5\times10^{-20}$ m$^2$ W$^{-1}$), SiN ($n_2 \sim 2.5\times10^{-19}$ m$^2$ W$^{-1}$) [18], and SiC ($n_2 \sim 5\times10^{-18}$ m$^2$ W$^{-1}$).

There are several reasons why in our study we considered only the Kerr nonlinearity of diamond: *i*) The main characteristic of the waveguide investigated in our work is that it is made of diamond, so that we primarily investigate the influence of the optical nonlinearity of diamond on pulse propagation in such waveguides. *ii*) In principle, one could use a covering layer made of a different material or a waveguide configuration in which this layer is absent altogether, and therefore there could be many potential contributions to the effective nonlinear optical coefficient of the waveguide. The particular configuration of the diamond waveguide studied in our paper was inspired by the results reported in Ref. [16], where the fabrication of such waveguides is discussed. *iii*) The optical mode is mostly confined in the diamond region, so that the contribution from the SiN layer can be omitted. Thus, whereas the confinement factor, $\kappa$, is smaller than in the SOI configuration, where $\kappa > 0.95$ can be readily achieved, a confinement factor $\kappa > 0.7$ can still be obtained without even trying to optimize the waveguide configuration. Moreover, the fact that a relatively small amount of optical field spills into the SiN region does not negatively affect the nonlinear optical properties of the waveguide because SiN has a large Kerr coefficient, too, and therefore the optical field that propagates in the SiN region contributes to nonlinearly induced phase shifts. *iv*) Finally, the contribution of the silica region to the waveguide nonlinearity can be neglected, too, since the Kerr nonlinearity of silica is much weaker than that of diamond. As a consequence of all these ideas, the overlap integrals in Eq. (2) were restricted to the diamond cross-section area.

The frequency dependence of the nonlinear coefficient, $\gamma$, and waveguide loss coefficient $\alpha = c\kappa\alpha_{in}/(2n_{di}v_g)$ defined in Eq. (2) are shown in Fig. 4. Note that the mode confinement decreases (less of the optical field is contained inside the waveguide) as the wavelength increases, a property that affects both waveguide coefficients. This is true particularly in the case of the waveguide with the smallest transverse cross-section (*A*, blue curves), whose coefficients $\gamma$ and $\alpha$ decrease significantly when the wavelength increases.
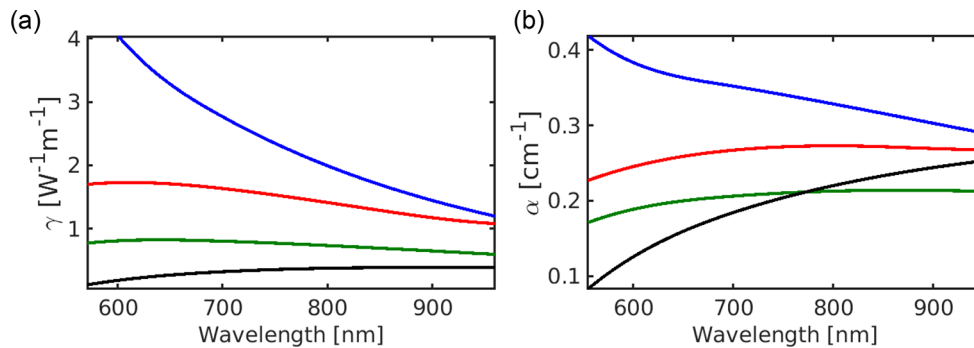


**Fig. 4.** (a) Frequency dispersion of the nonlinear waveguide coefficient. (b) Waveguide loss coefficient vs. wavelength. The colors blue, red, green, and black correspond to designs *A*, *B*, *C*, and *D*, respectively.

The data presented in Fig. 4 also guided our choice for the waveguide design we considered in more detail in our study. Thus, to be suitable for nonlinear optical applications, a waveguide must have large nonlinear optical coefficient and small loss coefficient. Among our four waveguides the design *B* best satisfies these requirements, so that in what follows we restrict our analysis to this waveguide.

Before discussing applications of these diamond fin waveguides, we would like to explain why we can neglect the influence on pulse dynamics of two nonlinear optical effects often included in the NLSE (1), namely the self-steepening (SS) effect and stimulated Raman scattering (SRS). To this end, let us consider first the contribution of SS effects to the pulse evolution. Following the

approach introduced in [22], we calculated the shock time, $\tau_s = \dfrac{\partial ln(\gamma)}{\partial \omega}$, which quantifies the strength of SS effects. To do this, we have included in the calculation of the nonlinear waveguide coefficient $\gamma$ the contribution of the material dispersion $n_2(\omega)$, taken from [23] and plotted in Fig. 5(a), as well as that of the waveguide dispersion shown in Fig. 4(a). The results of these calculations are depicted in Fig. 5(b). They demonstrate that $\tau_s \lesssim 0.6$ fs, which means that for pulses with width of tens of fs, as those considered in this work, SS effects can be neglected.

(a)

(b)
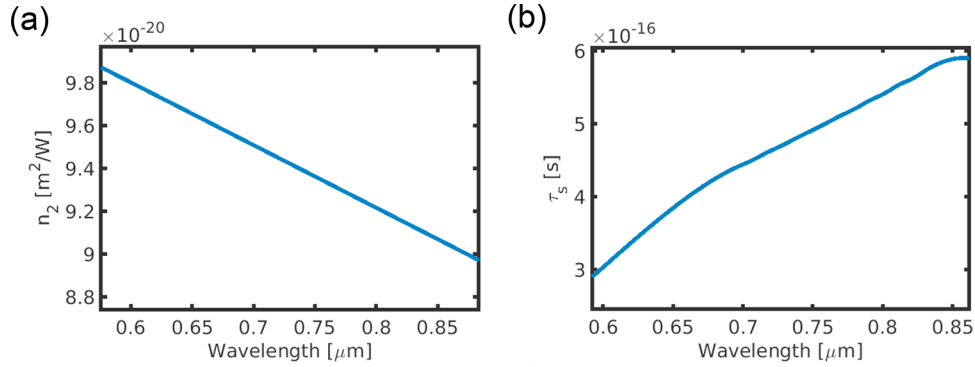


**Fig. 5.** (a) Dependence on wavelength of the nonlinear refractive index $n_2$ of diamond. (b) Shock time parameter of the diamond waveguide (design *B*), with contributions from both material and waveguide dispersion being included.

Furthermore, we have similarly assessed the relevance of the SRS effects on pulse dynamics by calculating the characteristic time $T_R$, which quantifies the Raman effect contribution to pulse reshaping. Specifically, this contribution can be accounted for by adding to (1) the term $-\gamma P_0 \dfrac{T_R}{T_0} u \dfrac{\partial |u|^2}{\partial \tau}$, where $T_0$ and $T_R = \int_0^\infty t R(t) dt$ are the pulse width and the first moment of the nonlinear response function, $R(t)$, respectively. Using the expression given in [24] for the nonlinear response function $R(t)$ of diamond, we obtain the following relation:

$$T_R = \int_0^\infty t R(t) dt = \frac{2\tau_2}{1 + (\frac{\tau_2}{\tau_1})^2} \sim 2 \frac{\tau_1^2}{\tau_2}, \tag{3}$$

where the parameters $\tau_1 \approx 4$ fs and $\tau_2 \approx 5.7$ ps are the vibrational period and the decay time of the Raman response in diamond, respectively. Using these specific values of $\tau_1$ and $\tau_2$ in Eq. (3) and a pulse with $T_0 = 10$ fs one obtains $\dfrac{T_R}{T_0} = 5.6 \times 10^{-4} \ll 1$. This leads us to conclude that the SRS effects can be neglected, too. By comparison, in the case of optical fibers and for the same pulse parameters $\dfrac{T_R}{T_0} = 0.81$ (for optical fibers $\tau_1 \approx 12.2$ fs and $\tau_2 \approx 32$ fs), which explains why in that case SRS effects must be incorporated in the theoretical model.

## 4. Applications to soliton formation and frequency comb generation

In what follows, we will illustrate how the diamond-fin waveguides analyzed in the preceding section can be used to implement important nonlinear optics applications, namely pulse reshaping, soliton generation, and frequency comb generation. To begin with, we consider the waveguide design *B* and select the wavelength $\lambda = 665$ nm, which is in the anomalous dispersion regime ($\beta_2 < 0$) but close to the zero-GVD point. This ensures that key nonlinear optical phenomena, such as soliton formation and supercontinuum generation, can be achieved. At this wavelength, the waveguide parameters are $n_g = c/v_g = 2.5$, $\beta_2 = -0.043$ ps$^2$ m$^{-1}$, $\beta_3 = -5.6 \times 10^{-5}$ ps$^3$ m$^{-1}$, $\alpha = 0.262$ cm$^{-1}$, and $\gamma = 1.687$ W$^{-1}$ m$^{-1}$. Using these parameters, we first determined the

pulse dynamics in a waveguide with length $L_{wg}$ = 5 cm, by integrating Eq. (1) with the standard split-step Fourier method [25]. More specifically, we seek to determine the input pulse parameters, i.e $P_0$ and $T_0$, for which phenomena such as soliton formation and spectral broadening occur.

The temporal pulse profiles calculated for several *z*-distances are depicted in Fig. 6(a). These calculations correspond to a case when we launched in the waveguide a Gaussian pulse with input peak power larger than the soliton formation threshold power. Specifically, we chose an input pulse width of $T_0$ = 25 fs, meaning that the dispersion length is $L_D = T_0^2/|\beta_2| = 1.5$ cm$<L_{wg}$, and input power $P_0$ = 60 W. Under these conditions, the power threshold for soliton formation, defined by the relation $L_D = L_{nl}$, where $L_{nl} = 1/(\gamma P_0)$ is the nonlinearity length, is $P_{th} = 40$ *textrmW*$<P_0$. These numerical simulations show that the input pulse evolves into a soliton superimposed on a pedestal, that is the well-known scenario of soliton formation at peak powers larger than the soliton threshold power. Note that for our parameters $L_{wg} \ll L_D'$, where $L_D' = T_0^3/|\beta_3| = 28$ cm is the TOD length, so that the pulse shape remains symmetric upon propagation.
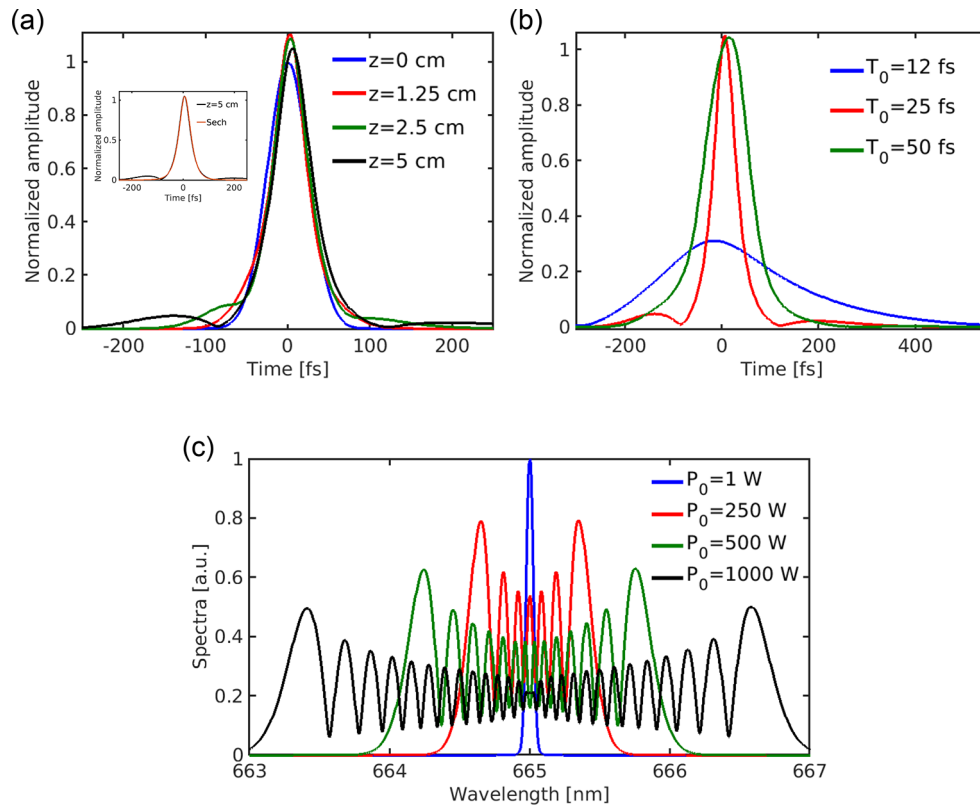


**Fig. 6.** (a) Temporal pulse profiles at different propagation lengths for a Gaussian input pulse with $P_0$ = 60 W and $T_0$ = 25 fs. Inset shows the output pulse and its sech-fit. (b) Output pulse profile determined for different pulse widths and $P_0$ = 60 W. (c) Output pulse spectra for different input peak powers when $T_0$ = 10 ps. In all cases, $L_{wg}$ = 5 cm.

In Fig. 6(b) we illustrate how the temporal pulse profile at the waveguide output changes when varying the input pulse width. Thus, when $T_0$ = 12 fs, the dispersion length ($L_D$ = 0.3 cm) is considerably smaller than $L_{nl}$ and $L_{wg}$, which means that large pulse broadening is achieved. In addition, $L_D'$ = 3 cm$<L_{wg}$, so that TOD effects lead to pulse asymmetry. By contrast, when $T_0$ = 50 fs, $L_D$ = 5.8 cm is comparable with $L_{wg}$, meaning that in this case both dispersive and nonlinear effects influence the pulse dynamics. Furthermore, we illustrate in Fig. 6(c) that

significant pulse spectral broadening can be achieved in the same waveguide length by using broader input pulses with larger input peak power, so that SPM effects become dominant in determining the pulse evolution. For example, the emergence of spectral modulations upon pulse propagation, for a pulse with $T_0 = 10$ ps can be clearly observed when the pulse peak power increases from 1 W to 1 kW.

From a practical point of view, perhaps an even more important application of diamond-fin waveguides, which we demonstrate in what follows, is frequency comb generation. This nonlinear optical phenomenon can be traced to the generation of dissipative solitons in optically driven Kerr cavities [27–31]. In particular, the nonlinear partial differential equation describing the evolution of the slowly-varying envelope of the electric component of an optical field propagating in an optical material with Kerr nonlinearity and driven by a continuous-wave (CW) monochromatic optical field, the so-called Lugiato-Lefever equation (LLE), was first derived in the context of optically driven nonlinear optical cavities [32] and shown to govern the generation of dissipative solitons. The temporal version of the LLE has been formulated in [33] and later extended to optical cavities containing nonlinear left-handed materials [34]. Its generalisation to an externally pumped NLSE with boundary conditions, a model relevant to the device we will investigate in what follows, has been first derived in [35].

To demonstrate frequency comb generation in a diamond-waveguide device as the one shown in Fig. 1(c), we consider a microring resonator of length $L$ coupled to a straight optical bus, both made of diamond-fin waveguides. The boundary conditions for our model are provided in Fig. 1(c), whereas the externally pumped NLSE describing the pulse propagation in the microring [36] (and which establishes a link between the dissipative soliton formation and frequency comb generation) is given below:

$$\frac{t_r}{L}\frac{\partial a(t,\tau)}{\partial t} = \frac{\sqrt{\theta}}{L}a_{in}(\tau) - \frac{\alpha' + i\delta}{L}a(t,\tau) - \frac{1}{v_g}\frac{\partial a(t,\tau)}{\partial \tau} - \frac{i\beta_2}{2}\frac{\partial^2 a(t,\tau)}{\partial \tau^2}$$
$$+ \frac{\beta_3}{6}\frac{\partial^3 a(t,\tau)}{\partial \tau^3} + i\gamma|a(t,\tau)|^2 a(t,\tau). \tag{4}$$

In this equation, the variable $z$ has been substituted by a temporal variable equivalent to a number $m$ of roundtrips, i.e. $t = mt_r$, $\alpha' = (\alpha_r + \theta)/2$, with $\alpha_r = \alpha L$, $\theta$ is the coupling constant of the driving field into the microring, and $\delta$ is the detuning of the microring resonance closest to the frequency of the driving field. The associated boundary conditions describe the coherent superposition of the field incoming from the pump and the field propagating inside the microring. More precisely, they show that the field starting the round $m + 1$ can be viewed as being equal to the in-coupled pump field plus the part of the field from the previous round $m$ that has not escaped out of the microring. This latter field has accumulated with respect to the pump field during the round trip the linear phase $\phi_0$.

The steady-state solution of Eq. (4) consists of a train of solitons with repetition time equal to the cavity round-trip time. This is equivalent to a comb in the frequency domain, with a frequency-spectral-range equal to the inverse of the round-trip time. To find the steady-state solution of Eq. (4), we impose the condition $\frac{\partial a(t,\tau)}{\partial t} = 0$. The resulting equation, whose solution only depends on $\tau$, is solved by combining a discrete Fourier transform (DFT) method with the Newton-Raphson algorithm for solving nonlinear systems of equations. It is important to note that the DFT method requires the use of wavelength dependent waveguide coefficients, so that the coefficients $c/v_g$, $\beta_2$, $\beta_3$, $\gamma$, and $\alpha$ are incorporated in the numerical method as wavelength dependent functions.

Following this approach, we considered a microring resonator based on waveguide $B$, of length $L = 628$ µm and operating at $\lambda = 665$ nm. For simplicity, we assumed that the system operates in the critical coupling regime, i.e. $\theta = \alpha_r$, and the detuning parameter was set to $\delta = 0.05$. Note this assumption can be justified as the microring radius of 100 µm is large enough to

avoid a tight coupling gap spacing, and especially narrower than the fin width, by comparing it with smaller microrings found in the literature [26]. The spectra and pulse shapes are shown in Figs. 7(a) and 7(b), respectively. They demonstrate that diamond-fin waveguides can be used to generate frequency combs in visible range reaching close to one octave-span. The pulse train building up inside the microring sits onto a CW background and has width of ~15 fs. Achieving such short pulses is made possible by the large nonlinearity ($\gamma$) of the system, which induces significant spectral broadening and thus the excitation of a large number of optical modes of the microring. Our simulations reveal that the lowest input power required to reach the steady state is $P_{in} \approx 0.5$ W. When $P_{in}$ increases, the comb is hardly affected, but the driving wavelength is slightly redshifted. In the time domain, increased $P_{in}$ leads to larger CW background.
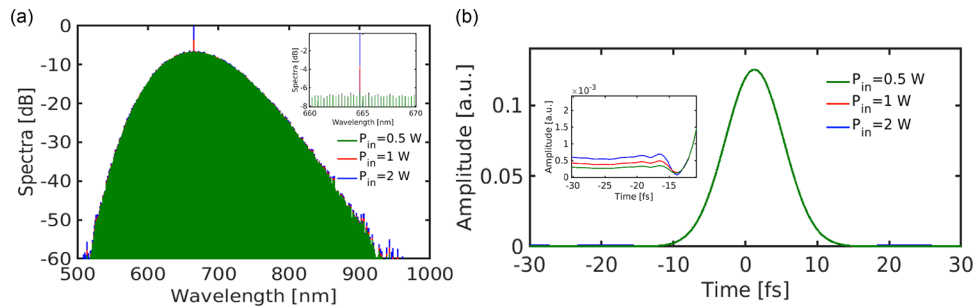


**Fig. 7.** (a) Simulated frequency comb spectra for a microring of length $L = 628$ μm based on waveguide design *B*. The inset demonstrates the flatness of the comb around the driving wavelength. (b) Temporal pulse profile within the microring. The inset shows the variation of the CW background intensity with the input power.

As a final observation, we mention that the NLSE Eq. (4) can be used directly to investigate the formation and evolution of the comb towards its stationary state [36], but this method would have required considerably more computational time without gaining much in return. Inasmuch as our study is geared towards applications to nonlinear optics of ultrasmall diamond waveguides, the specific nature of the soliton formation during the build-up process is not particularly relevant for the properties of the final frequency comb that is generated. In fact, this is why we chose to employ in our simulations a numerical method tailored for computing directly the steady-state solution, and as such a method not suitable for the analysis of the transient regime. The advantage of our method, which is particularly relevant for practical application, is that it allows one to investigate extremely broad frequency combs as a very large number of spectral modes can be incorporated at minimum computational cost.

## 5. Conclusions

To conclude, we have presented the design of diamond-fin waveguides and analyzed in detail their linear and nonlinear optical properties. In particular, we have determined the frequency dependence of the main linear and nonlinear optical coefficients of the waveguides and analyzed the dependence of these parameters on the waveguide geometry. By selecting one of the proposed waveguide designs with optimum characteristics, we have simulated the pulsed dynamics through these structures by means of a comprehensive mathematical model based on NLSE. The results of our investigations suggest that these structures can enable efficient soliton formation and propagation and, potentially, supercontinuum generation. In addition, we have demonstrated how these waveguides can be employed to generate frequency combs operating in the visible spectral domain. Importantly, our simulations show that it is possible to generate almost one octave span stable combs in the visible range with input continuous-wave powers as low as 0.5 W.

**Disclosures.** The authors declare no conflicts of interest.

**Data availability.** Data underlying the results presented in this paper are not publicly available at this time but may be obtained from the authors upon reasonable request.

## References

1. R. Mildren and J. Rabeau, *Optical Engineering of Diamond* (Wiley-VCH, 2013).
2. I. Aharonovich, A. D. Greentree, and S. Prawer, "Diamond photonics," Nat. Photonics **5**(7), 397–405 (2011).
3. B. J. M. Hausmann, I. Bulu, V. Venkataraman, P. Deotare, and M. Loncar, "Diamond nonlinear photonics," Nat. Photonics **8**(5), 369–374 (2014).
4. P. Latawiec, V. Venkataraman, M. J. Burek, B. J. M. Hausmann, I. Bulu, and M. Loncar, "On-chip diamond Raman laser," Optica **2**(11), 924–928 (2015).
5. T. Schröder, S. L. Mouradian, J. Zheng, M. E. Trusheim, M. Walsh, E. H. Chen, L. Li, I. Bayn, and D. Englundr, "Quantum nanophotonics in diamond [Invited]," J. Opt. Soc. Am. B **33**(4), B65–B83 (2016).
6. R. Halir, P. J. Bock, P. Cheben, A. Ortega-Monux, C. Alonso-Ramos, J. H. Schmid, J. Lapointe, D. X. Xu, J. G. Wanguemert-Perez, I. Molina-Fernandez, and S. Janz, "Waveguide sub-wavelength structures: a review of principles and applications," Laser Photonics Rev. **9**(1), 25–49 (2015).
7. R. M. Osgood, N. C. Panoiu, J. I. Dadap, X. Liu, X. Chen, I-W. Hsieh, E. Dulkeith, W. M. J. Green, and Y. A. Vlassov, "Engineering nonlinearities in nanoscale optical systems: physics and applications in dispersion-engineered silicon nanophotonic wires," Adv. Opt. Photonics **1**(1), 162–235 (2009).
8. D. J. Blumenthal, R. Heideman, D. Geuzebroek, A. Leinse, and C. Roeloffzen, "Silicon Nitride in Silicon Photonics," Proc. IEEE **106**(12), 2209–2231 (2018).
9. L. Chang, G. D. Cole, G. Moody, and J. E. Bowers, "CSOI: Beyond Silicon-on-Insulator Photonics," Opt. Photonics News **33**(1), 24–32 (2022).
10. J. A. Tatum, D. Gazula, L. A. Graham, J. K. Guenter, R. H. Johnson, J. King, C. Kocot, G. D. Landry, I. Lyubomirsky, A. N. MacInnes, E. M. Shaw, K. Balemarthy, R. Shubochkin, D. Vaidya, M. Yan, and F. Tangr, "VCSEL-Based Interconnects for Current and Future Data Centers," J. Lightwave Technol. **33**(4), 727–732 (2015).
11. M. Burek, Y. Chu, M. S. Z. Liddy, P. Patel, J. Rochman, S. Meesala, W. Hong, Q. Quan, M. D. Lukin, and M. Loncar, "High quality-factor optical nanocavities in bulk single-crystal diamond," Nat. Commun. **5**(1), 5718 (2014).
12. A. L. Gaeta, M. Lipson, and T. J. Kippenberg, "Photonic-chip-based frequency combs," Nat. Photonics **13**(3), 158–169 (2019).
13. W. Bogaerts, P. De Heyn, T. Van Vaerenbergh, K. De Vos, S. Kumar Selvaraja, T. Claes, P. Dumon, P. Bienstman, D. Van Thourhout, and R. Baets, "Silicon microring resonators," Laser Photonics Rev. **6**(1), 47–73 (2012).
14. J. Liu, E. Lucas, A. S. Raja, J. He, J. Riemensberger, R. N. Wang, M. Karpov, H. Guo, R. Bouchand, and T. J. Kippenberg, "Photonic microwave generation in the X- and K-band using integrated soliton microcombs," Nat. Photonics **14**(8), 486–491 (2020).
15. L. W. Luo, N. Ophir, C. P. Chen, L. H. Gabrielli, C. B. Poitras, K. Bergmen, and M. Lipson, "WDM-compatible mode-division multiplexing on a silicon chip," Nat. Commun. **5**(1), 3069 (2014).
16. R. R. Grote and L. C. Bassett, "Single-mode optical waveguides on native high-refractive-index substrates," APL Photonics **1**(7), 071302 (2016).
17. A. Shams-Ansari, P. Latawiec, Y. Okawachi, V. Venkataraman, M. Yu, B. Desiatov, H. Atikian, G. L. Harris, N. Picque, A. L. Gaeta, and M. Loncarr, "Supercontinuum generation in angle-etched diamond waveguides," Opt. Lett. **44**(16), 4056–4059 (2019).
18. FemSIM, www.synopsys.com.
19. X. Chen, N. C. Panoiu, and R. M. Osgood, "Theory of Raman-Mediated Pulsed Amplification in Silicon-Wire Waveguides," IEEE J. Quantum Electron. **42**(2), 160–170 (2006).
20. N. C. Panoiu, J. F. McMillan, and C. W. Wong, "Theoretical Analysis of Pulse Dynamics in Silicon Photonic Crystal Wire Waveguides," IEEE J. Sel. Top. Quantum Electron. **16**(1), 257–266 (2010).
21. K. Ikeda, R. E. Saperstein, N. Alic, and Y. Fainman, "Thermal and Kerr nonlinear properties of plasma-deposited silicon nitride/silicon dioxide waveguides," Opt. Express **16**(17), 12987–12994 (2008).
22. N. C. Panoiu, X. Liu, and R. M. Osgood, "Self-steepening of ultrashort pulses in silicon photonic nanowires," Opt. Lett. **34**(7), 947–949 (2009).
23. J. M. P. Almeida, C. Oncebay, J. P. Siqueira, S. R. Muniz, L. De Boni, and C. R. Mendonca, "Nonlinear optical spectrum of diamond at femtosecond regime," Sci. Rep. **7**(1), 14320 (2017).
24. T. M. Kardas, B. Ratajska-Gadomska, W. Gadomski, A. Lapini, and R. Righinir, "The role of stimulated Raman scattering in supercontinuum generation in bulk diamond," Opt. Express **21**(20), 24201–24209 (2013).
25. G. P. Agrawal, *Nonlinear Fiber Optics* (Academic Press, 2001).
26. A. J. Scroggie, W. J. Firth, G. S. McDonald, M. Tlidi, R. Lefever, and L. A. Lugiato, "Pattern formation in a passive Kerr cavity," Chaos, Solitons Fractals **4**(8-9), 1323–1354 (1994).

27. M. Tlidi and L. Gelensr, "High-order dispersion stabilizes dark dissipative solitons in all-fiber cavities," Opt. Lett. **35**(3), 306–308 (2010).

28. M. Tlidi, L. Bahloul, L. Cherbi, A. Hariz, and S. Coulibaly, "Drift of dark cavity solitons in a photonic-crystal fiber resonator," Phys. Rev. A **88**(3), 035802 (2013).

29. A. G. Vladimirov, S. V. Gurevich, and M. Tlidi, "Effect of Cherenkov radiation on localized-state interaction," Phys. Rev. A **97**(1), 013816 (2018).

30. A. G. Vladimirov, M. Tlidi, and M. Taki, "Dissipative soliton interaction in Kerr resonators with high-order dispersion," Phys. Rev. A **103**(6), 063505 (2021).

31. L. A. Lugiato and R. Lefever, "Spatial Dissipative Structures in Passive Optical Systems," Phys. Rev. Lett. **58**(21), 2209–2211 (1987).

32. M. Haelterman, S. Trillo, and S. Wabnitz, "Dissipative modulation instability in a nonlinear dispersive ring cavity," Opt. Commun. **91**(5-6), 401–407 (1992).

33. P. Kockaert, P. Tassin, G. Van der Sande, I. Veretennicoff, and M. Tlidi, "Negative diffraction pattern dynamics in nonlinear cavities with left-handed materials," Phys. Rev. A **74**(3), 033822 (2006).

34. M. Tlidi, A. Mussot, E. Louvergneaux, G. Kozyreff, A. G. Vladimirov, and M. Takir, "Control and removal of modulational instabilities in low-dispersion photonic crystal fiber cavities," Opt. Lett. **32**(6), 662–664 (2007).

35. S. Coen, H. G. Randle, T. Sylvestre, and M. Erkintalo, "Modeling of octave-spanning Kerr frequency combs using a generalized mean-field Lugiato-Lefever model," Opt. Lett. **38**(1), 37–39 (2013).

36. T. Christopoulos, O. Tsilipakos, N. Grivas, and E. E. Kriezis, "Coupled-mode-theory framework for nonlinear resonators comprising graphene," Phys. Rev. E **94**(6), 062219 (2016).